# Numerical modelling of three-dimension stress rotation ahead of an advancing tunnel face

E. Eberhardt*

*Engineering Geology, Swiss Federal Institute of Technology Zürich, ETH Hönggerberg, CH 8093 Zürich, Switzerland*

## Abstract

As underground excavations and construction works progress into deeper and more complex geological environments, understanding the three-dimensional redistribution of excavation-induced stresses becomes essential given the adverse consequences such stresses will have on the host rock strength and the subsequent excavation stability. This paper presents the results from a detailed three-dimensional finite-element study, which explores near-field stress paths during the progressive advancement of a tunnel face. These results demonstrate that as the tunnel face approaches and passes through a unit volume of rock, the spatial and temporal evolution of the three-dimensional stress field encompasses a series of deviatoric stress increases and/or decreases as well as several rotations of the principal stress axes. Particular emphasis is placed on the rotation of the principal stress axes as being a controlling factor in the direction of fracture propagation. If this orientation changes in time, i.e. during the progressive advancement of the tunnel face, the type of damage induced in the rock mass and the resulting failure mechanisms may also vary depending on the type and degree of stress rotation. The significance of these effects is discussed in terms of microfracture initiation and propagation, brittle fracture damage and rock strength degradation. Further analysis is also presented for varying tunnelling conditions including the effects of tunnel alignment with respect to the initial in situ stress field, excavation sequencing and elasto-plastic material yielding. Implications with respect to the new Gotthard base tunnel, currently under construction in Switzerland, are presented using examples from the nearby Furka tunnel. © 2001 Elsevier Science Ltd. All rights reserved.

## 1. Introduction

In a stressed rock mass, the sequencing and advancement of a tunnel face results in the disturbance and redistribution of the primary in situ stress field. This disturbance involves both changes in magnitude and orientation of the stress-field tensor in the proximity of the tunnel boundary (referred to as the near-field). Moving away from the tunnel boundary, the stress tensor eventually returns to its initial in situ state (i.e. in the far-field). Given the controlling influence that stress magnitude and orientation plays in the development of brittle fractures, rock strength degradation (i.e. damage) and rock mass instabilities, the analysis of such changes has become standard practice in most rock excavation designs.

The analysis of excavation-induced stresses has, in the past, been primarily restricted to two-dimensions (e.g. plane strain). Such constraints require that the problem geometry be represented as a cross-section perpendicular to the excavation axis, around which the near-field stress trajectories, representing the major and minor principal stresses ($\sigma_1$ and $\sigma_3$, respectively), can be visualised as "flowing" (Fig. 1). In general, two-dimensional representations have dominated both analytical and numerical solutions, and constitute the majority of boundary-element, finite-element and distinct-element codes commercially available.

The two-dimensional assumption, however, is inadequate if three-dimensional effects are considered to be significant. Eberhardt et al. [1] and Meyer et al. [2] have demonstrated that three-dimensional analysis, utilising numerical modelling techniques, allows for a more detailed examination of the near-field stress concentrations that develop around the ends and edges of an excavation. In the case of an advancing tunnel face, three-dimensional stress effects have been shown to be an important factor, especially with respect to induced stress concentrations and rock strength degradation [3–5].

*Tel.: +41-1-633-25-94; fax: +41-1-633-11-08.

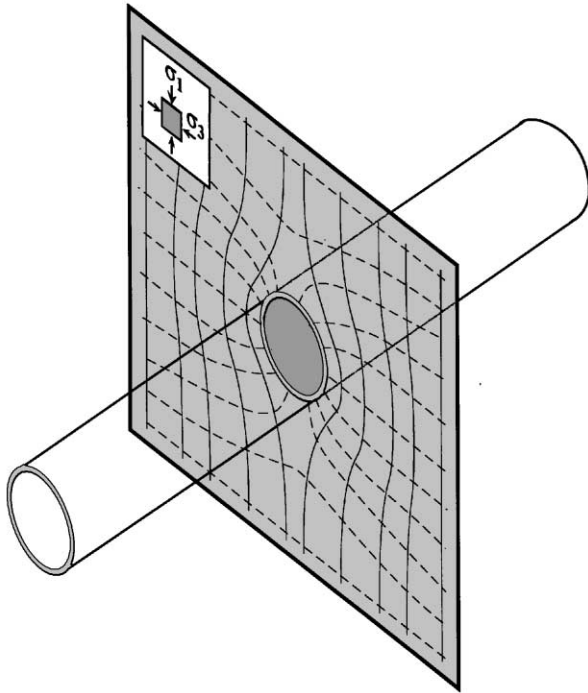*E-mail address:* erik@erdw.ethz.ch (E. Eberhardt).

Fig. 1. Two-dimensional flow of the principal stress trajectories around a circular opening.

As tunnelling projects continue to progress into deeper and more complex geological environments, e.g. the Gotthard and Lötschberg base tunnels currently under construction in central Switzerland [6], understanding the three-dimensional redistribution of excavation induced stresses becomes even more necessary given the adverse consequences such stress paths will have on the host rock strength. Of equal importance are the corresponding displacements, the extent of the damage and plastic zones ahead of the tunnel face, and the subsequent excavation stability. This paper presents the results from a detailed three-dimensional finite-element study, which explores the progressive development and evolution of induced near-field stresses and stress paths during the advancement of a tunnel face. The influence of tunnel alignment with respect to the primary in situ stress directions, excavation sequencing and elasto-plastic displacements are considered. The analyses concentrate on both changes in stress magnitudes and the rotation of the principal stress axes as a tunnel excavation approaches and passes through a unit volume of rock. The significance of these effects will be subsequently discussed with respect to brittle fracture propagation, induced damage and rock strength degradation. Observations of stress-induced slabbing and spalling from the Furka tunnel access adit ''Fenster Bedretto'' in the central Swiss Alps will be used.

## 2. Stress effects ahead of an advancing tunnel face

The redistribution of near-field stresses following tunnel excavation have been studied extensively using a number of analytical, physical and numerical modelling techniques. Predominantly two-dimensional in nature, these studies often concentrate on stresses, displacements and stability (e.g. factor of safety) in the tunnel's crown and walls. The assumption of plane strain is typically employed in two-dimensional analyses, requiring that the out-of-plane stress coincides with the intermediate principal stress, $\sigma_2$, and that the problem geometry being analysed is long and of regular cross-section in the out-of-plane direction. This means that the ends of the excavation are assumed to be of considerable distance away from the tunnel section being analysed, thereby excluding the possibility of analysing the excavation-induced stresses at the tunnel face.

Duddeck [7] notes that if the engineering design requires knowledge of the induced stresses and deformations of the tunnel structure, the geometrical changes at the working face and the sequences of excavation and support must be considered. Studies by Pan and Hudson [8] and Kielbassa and Duddeck [9] have shown that two-dimensional plane strain models, in direct comparison to their three-dimensional equivalents, are inadequate when modelling stresses and tunnel convergence near the tunnel face and must be corrected to account for stress redistribution and excavation sequencing. Although more complexity is added by considering the third dimension (the added dimension being parallel to the long axis of the excavation), the modelled interaction between excavation-induced stresses and rock mass response near and ahead of the tunnel face becomes possible. Several studies have emphasised the importance of such investigations, in terms of tunnel convergence [10], rock-support interaction [9,11–12], excavation disturbance/damage zone [5], borehole breakout [13], prediction of changing ground conditions [14] and tunnel face instability [4].

Through these studies, the zone of influence generated by an advancing tunnel face can be shown to be significant and far-reaching (in general, several tunnel diameters). Abel and Lee [3], for example, report detectable stress changes 2–4 diameters ahead of a tunnel face as measured in laboratory simulations of incremental tunnel advancements through blocks of acrylic, concrete and granite. In the same study, stress changes were detected 7.5 diameters ahead of a crosscut at an experimental mine situated in a jointed, gneissic granite. Martin et al. [15], during experiments at the URL in Canada, found that the in situ strength of the near-field rock decreased by half its laboratory strength due to brittle fracture damage induced by the stress path acting ahead of the tunnel face. Such changes

to the rock mass conditions (e.g. elastic modulus, cohesive strength, etc.) will ultimately influence the near-field tunnel deformation mechanisms and modes of failure. A further consequence is that the material properties measured during the site investigation phase could well be significantly altered during and after tunnel excavation.

## 3. Three-dimensional stress path analysis of sequential tunnel advancement

### 3.1. Model construction and analysis methodology

A series of three-dimensional finite-element models were constructed and solved for using the commercial code Visage [16]. The models were constructed using 5200 20-node brick elements assuming symmetry in a plane parallel to the tunnel axis (Fig. 2). Element sizes and aspect ratios were minimised near the tunnel boundary and gradually increased outwards. A tunnel diameter of 10 m was used with the outer boundary extending to a distance of 100 m to minimise boundary effects. An overburden of 1000 m was assumed, approximating conditions that will be seen over certain sections
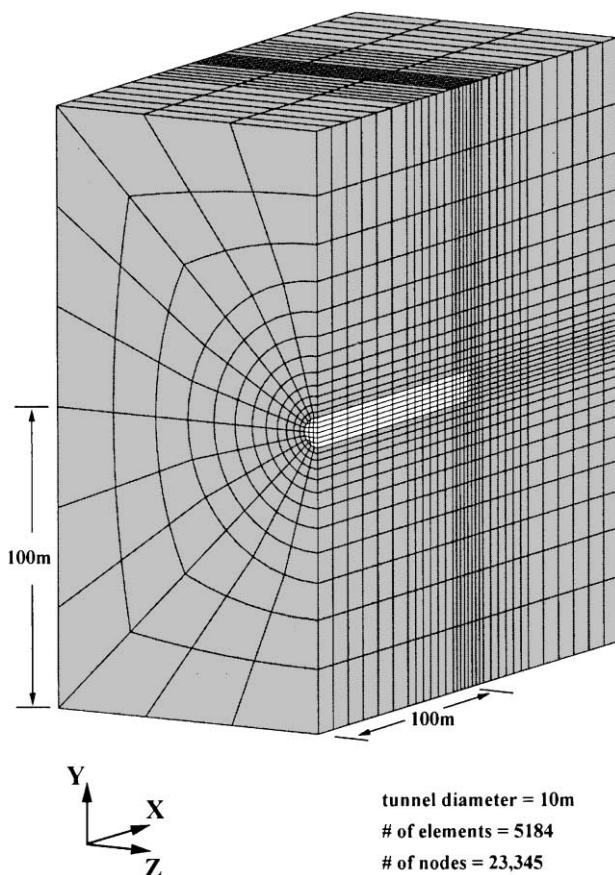
of the planned Gotthard base tunnel. Table 1 provides the material properties used in both the elastic and elasto-plastic model runs. These values were based on laboratory testing of granites from the Aar and Gotthard massifs in the central Swiss Alps [17]. Although rock strengths can approach those normally expected of competent, intact granites, low values of uniaxial compressive strength and cohesion arise owing to varying degrees of metamorphism and a high microfracture density related to either tectonic or hydro-thermal-mechanical processes experienced throughout portions of these massifs.

The models were constructed so as to simulate the progressive excavation of a cylindrical tunnel using two intermediate benches (i.e. an upper bench, followed by the excavation of a lower bench, Fig. 3). The stress path analysis was performed for each incremental advance of the tunnel face (21 stages in total) using an iterative solver. The calculation and analysis of stresses in a finite-element model can be readily performed using any arbitrary reference axes. In numerical modelling practice, the reference axes are often chosen such that the $x, y, z$ co-ordinate system of the model is parallel to the vertical and horizontal axes of the problem geometry (e.g. $\sigma_v$, $\sigma_{hmax}$, $\sigma_{hmin}$). A second non-arbitrary reference axes, the principal stress axes ($\sigma_1$, $\sigma_2$, $\sigma_3$), is also often used and corresponds to the normals to a set of orthogonal planes for which there are no active shear

Table 1
Finite-element input parameters used in three-dimensional tunnel models

| Model input parameter | Value |
|---|---|
| Density, $\rho$ | 2700 kg/m$^3$ |
| Young's modulus, E | 20 GPa |
| Poisson's ratio, $v$ | 0.25 |
| Intact cohesion, c | 10 MPa |
| Intact friction angle, $\phi_i$ | 30 |
| Tensile strength, $\sigma_t$ | 5 MPa |



Fig. 2. Three-dimensional finite-element mesh and model geometry.

tunnel diameter = 10m
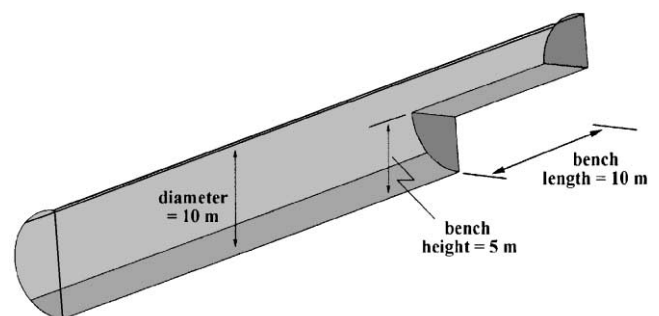# of elements = 5184
# of nodes = 23,345



Fig. 3. Excavation sequencing and tunnel bench dimensions as incorporated into numerical models.

stresses (i.e. the planes are only subjected to a normal component of stress). One of the advantages of analysing the excavation disturbed near-field stress zone in terms of principal stresses is that the microfracturing process, relating to damage and rock strength degradation/failure, is largely controlled by the deviatoric stresses and the orientation of the principal stress axes (e.g. [5,18–19]). These processes and their implications are discussed in more detail in later sections.

### 3.2. Stress paths along the tunnel boundaries and at the tunnel face

Stresses were analysed along the tunnel boundary and ahead of the face for several lines running parallel to the tunnel axis. The three-dimensional mesh was assembled so that these lines would coincide with the tunnel roof and walls, both on the tunnel boundary and along a parallel line 1 m into the rock mass, and along the centreline of the tunnel axis ahead of the working face. Based on this analysis methodology, several series of model runs were performed focussing on the influence

of the initial stress state with respect to the orientation of the tunnel axis and the effects of elasto-plastic material yield on stress redistribution, stress path and the rotation of the $\sigma_1$ stress axis. These results are presented in the following two sub-sections.

#### 3.2.1. In situ stress state

The first series of models solved for examined the influence of the orientation of the initial major principal stress, $\sigma_{1i}$, relative to the alignment of the tunnel axis

Table 2
Initial in situ stress states considered (with respect to the tunnel axis)

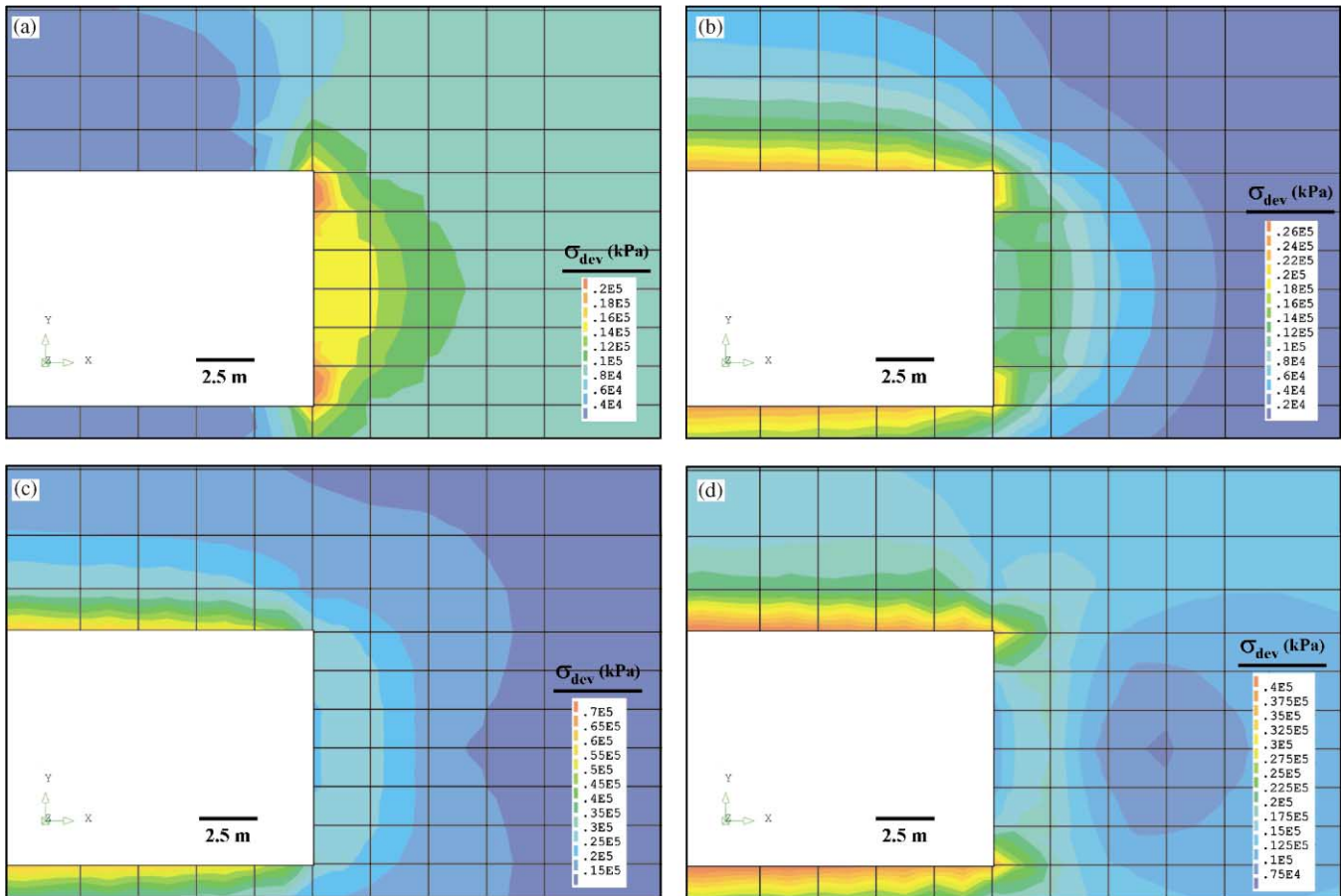| Model case | In situ vertical stress (MPa) | In situ horizontal stress (MPa) | |
| --- | --- | --- | --- |
| | | Parallel to tunnel axis | Perpendicular to tunnel axis |
| I | 27.0 | 13.5 | 9.0 |
| II | 27.0 | 27.0 | 27.0 |
| III | 27.0 | 40.5 | 54 |
| IV | 27.0 | 54 | 40.5 |



Fig. 4. Plots of the deviatoric stress contours, $\sigma_{dev}$, along the longitudinal tunnel profile (i.e. parallel to the tunnel axis) for each of the initial stress conditions outlined in Table 2: (a) Case I—lithostatic loading; (b) Case II—hydrostatic loading; (c) Case III—$\sigma_{1i}$ horizontal and perpendicular to tunnel axis; (d) Case IV—$\sigma_{1i}$ parallel to tunnel axis.

(note that the subscript "$i$" is used herein to refer to the *initial* principal stress field to avoid later confusion with the excavation-disturbed secondary stress field). In each case, the initial vertical stress was assumed to be equal to the overburden load with the far-field horizontal stresses, parallel and perpendicular to the tunnel axis, varying between 0.33 and 2.0 times this value (Table 2). In other words, a different $K$ value (i.e. horizontal/vertical stress ratio) was assumed so that the primary $\sigma_{1i}$ stress would be first aligned vertically (Case I) and then horizontally perpendicular (Case III) and parallel (Case IV) to the tunnel axis. In Case II, hydrostatic conditions were assumed (i.e. $K = 1$). Table 2 summarises the magnitudes and orientation of the initial principal stresses with respect to the tunnel alignment.

For each model run in this series, linear elasticity was assumed. Fig. 4 provides plots of the deviatoric stress, $\sigma_{\text{dev}}$, contours along the longitudinal tunnel profile (i.e. parallel to the tunnel axis) for each of the cases outlined in Table 2. In model Case I, the initial stress state represents that which is typically assumed for simple two-dimensional analyses, i.e. lithostatic loading, where $\sigma_1$ is vertical and equal to the overburden rock load, $\sigma_2$ is normal or "out-of-plane" to the two-dimensional tunnel cross-section and $\sigma_3$ is horizontally perpendicular to the tunnel axis and is estimated as a function of the Poisson's ratio. Results shown in Fig. 5 indicate that at distances greater than 5 m (i.e. 0.5 tunnel diameters) *behind* the working face, the deviatoric stresses in the

tunnel walls are higher than those in the roof. Nearer the tunnel face the deviatoric stresses in the roof significantly increase and surpass magnitudes calculated for the tunnel walls. *Ahead* of the tunnel face, stresses decrease but still maintain magnitudes 40%, 10% and 5% above those of the initial $\sigma_{\text{dev}}$ stress at distances of 1, 5 and 10 m, respectively.

This picture, however, provides only a static representation of the disturbed stress field at the tunnel face. Further insight may be gained by visualising the results in terms of following the stress path as the tunnel excavation approaches and passes through a unit volume of rock. Fig. 6 shows the principal stress magnitudes and orientations, based on the initial stress conditions of Case I, for two fixed points relative to the forward sequential advancement of the tunnel face (as shown in the central schematic illustration between the upper and lower plots). Fixed along the future position of the tunnel roof and wall, stress values calculated at these two points were averaged over the volume between the tunnel boundary and nodes 0.5 m into the rock mass. Moving from left to right in these plots (e.g. Fig. 6), the stress path can be followed as the tunnel face approaches the monitoring points ($-10$ to $0$ m) and passes by them ($0$ to $10$ m). The changing principal stress magnitudes within the fixed volumes can be read from the $y$-axis, whereas a small vector at each point represents the orientation of the principal stresses.
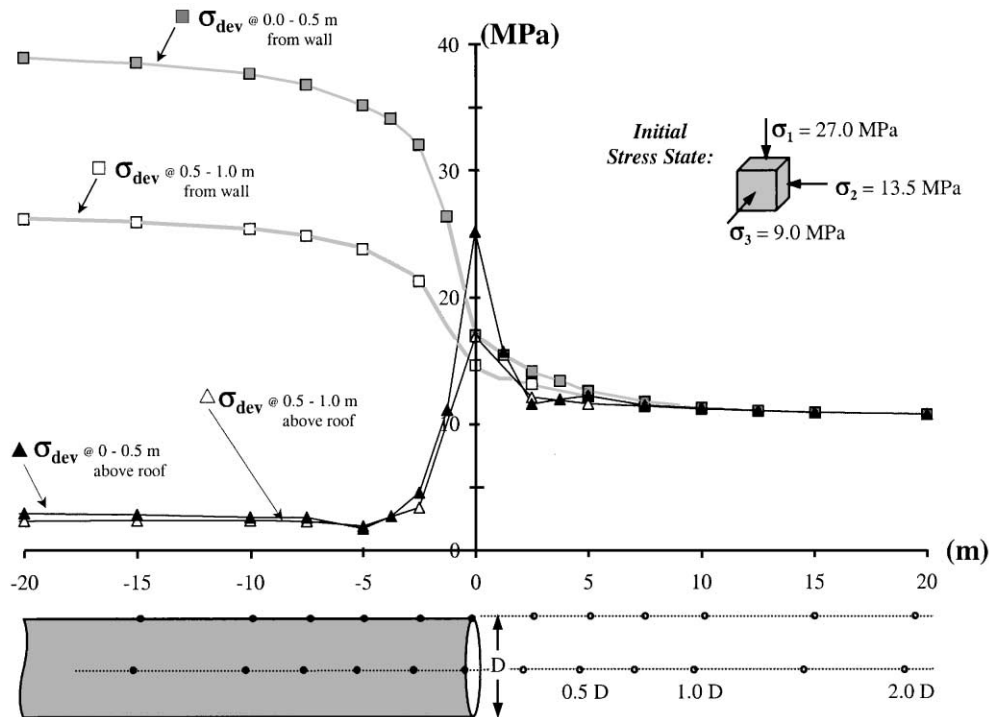


Fig. 5. Plots comparing $\sigma_{\text{dev}}$ stress magnitudes for points along and 1 m away from the tunnel roof and wall boundaries for a given position of the tunnel face, assuming the initial stress conditions for "Case I"—lithostatic loading.
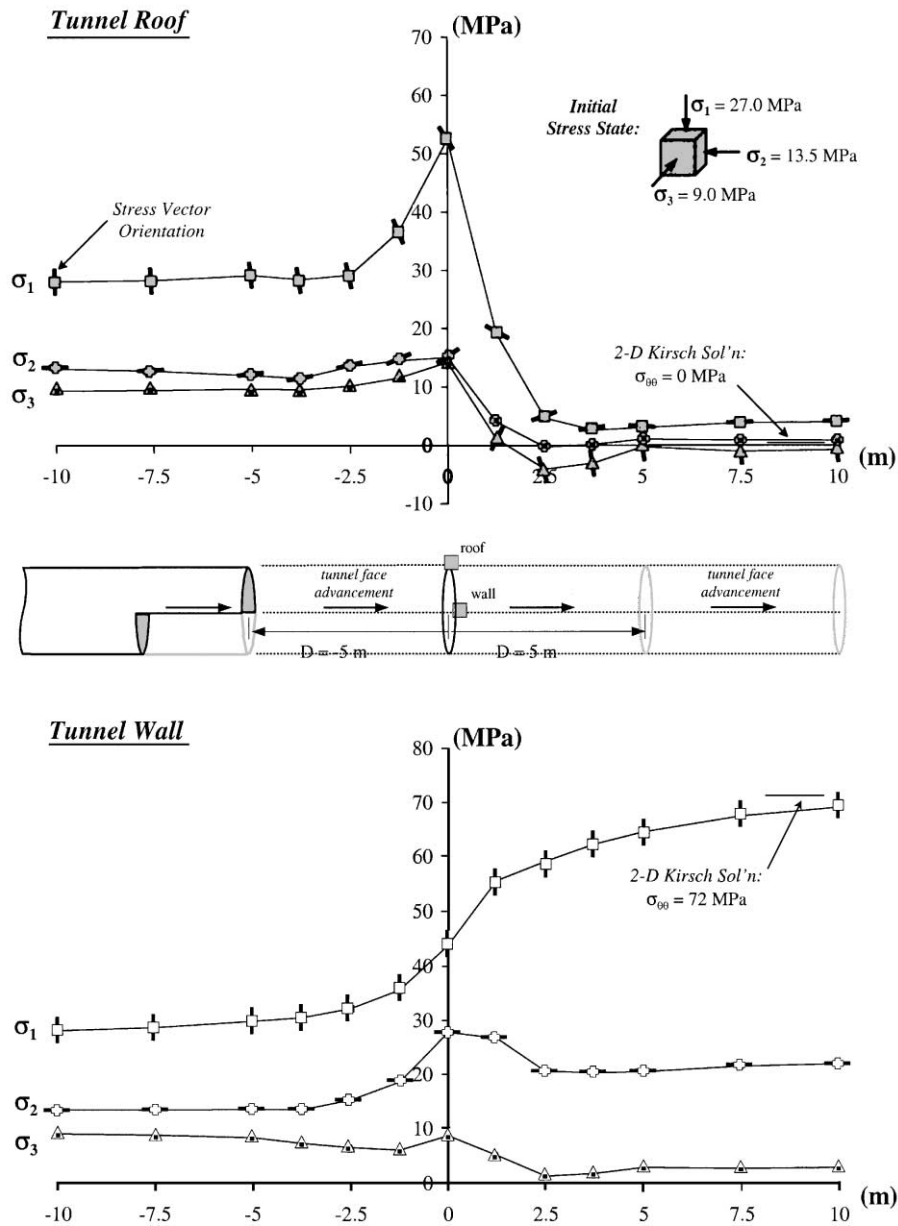
Fig. 6. Stress path plots of the principal stress magnitudes and orientations at fixed points in the tunnel roof (upper) and wall (lower) for initial stress state "Case I".

Accordingly, stress magnitudes in Fig. 6 begin to deviate from the far-field initial values as the tunnel face approaches the monitored rock volumes, and converge towards those that approximate the two-dimensional Kirsch solution [20] once the tunnel face passes by them. In terms of the principal stress axes orientation, the $\sigma_1$ stress vector gradually rotates from its initially vertical position, 10 m ahead of the tunnel face (i.e. at $-10$ m in the upper plot of Fig. 6), to a horizontal position parallel to the tunnel axis along the boundary of the tunnel roof. This rotation is complete once the face has advanced 5–10 m past the fixed monitoring point. In the tunnel walls, the $\sigma_1$ stress axis does not rotate from

vertical as the tangent to the tunnel wall coincides with vertical, but the orientations of the $\sigma_2$ and $\sigma_3$ axes do rotate in the horizontal plane as they bend around the edges of the tunnel face.

Tunnel roof and wall displacements can be viewed in a similar manner. Fig. 7 shows the total elastic displacements observed at the two fixed monitoring points in the tunnel roof and walls. Given the vertical orientation of the primary major principal stress, $\sigma_{1i}$, the largest displacements are observed in the tunnel roof. As shown on the left-hand side of the plot, displacements begin to accumulate before the tunnel face reaches the fixed monitoring points but are limited due to

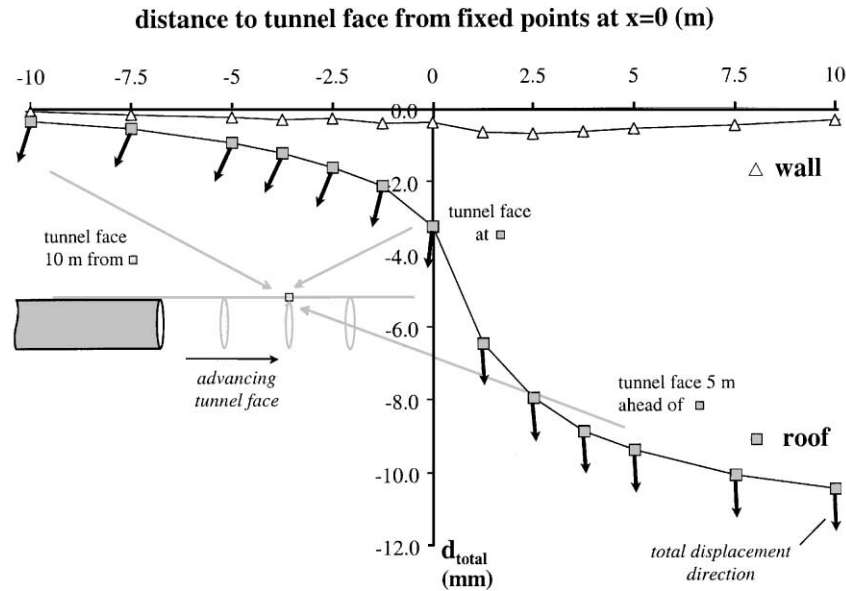**distance to tunnel face from fixed points at x=0 (m)**



Fig. 7. Accumulation of total elastic displacements with tunnel face advancement for fixed points in the tunnel roof (upper) and wall (lower) for initial stress state "Case I". Direction vectors are provided for the tunnel roof displacements.

confinement. Fig. 7 also provides the direction vectors for the displacements in the tunnel roof. Displacements, both in the tunnel walls and roof, begin by moving towards the approaching tunnel face, and then redirect themselves in the direction of the tunnel face as it passes by and moves further away from the fixed monitoring points. The angle towards which the displacements in the tunnel roof align themselves varies from 25° off vertical, 5 m before the tunnel face has reached the monitoring point, to 7° as the tunnel face reaches the monitoring point, to $-3°$ after the tunnel face has advanced 5 m past the fixed monitoring point.

Results for the other initial stress conditions described in Table 2 are presented in Figs. 8–10. Given certain unknowns regarding the primary stress conditions along several sections of the Gotthard base-tunnel, these initial stress conditions include those where the horizontal stresses equal or exceed vertical (i.e. $K = 1$ to $K > 1$). With the realignment of the primary $\sigma_1$ stress axis from vertical to horizontal, the excavation-induced stress conditions in the tunnel walls and roof reverse from those shown in Fig. 6 and the higher compressive stresses are found along the roof. The exception is the hydrostatic case, Case II (Fig. 8), where the stress conditions in the tunnel walls and roof are the same.

Similar to results for Case I (i.e. $K < 1$), the initial stress conditions at the beginning of the stress paths for Cases II, III and IV, are seen to vary little before the tunnel face approaches within 10 m of the fixed monitoring points. On the opposite end of the stress path plots, stress magnitudes converge towards those values approximated by the Kirsch solution once the tunnel face has moved more than 10 m past the monitoring points. An irregularity occurs in

Case IV, however, since the two-dimensional limitation of the Kirsch solution does not allow for an initial $\sigma_1$ stress acting parallel to the tunnel axis and therefore approximates the tangential stresses in the tunnel walls as being the $\sigma_2$ stress acting horizontally in the plane of the tunnel cross-section (Fig. 10, lower plot).

Inside 5 m of the working face, the stress paths for the different cases are seen to vary significantly. In Case III, where the initial $\sigma_1$ stress is horizontal and perpendicular to the tunnel axis, the induced deviatoric stress values in the tunnel roof increase both as the tunnel face approaches and passes by the monitoring point. However, the orientation of the $\sigma_1$ axis does not vary from its initial position of horizontal and normal to the tunnel axis, and only the $\sigma_2$ and $\sigma_3$ axes show slight rotations as the tunnel face advances past the monitoring point (Fig. 9, upper plot). In the tunnel walls of Case III (Fig. 9, lower plot), deviatoric stresses increase sharply as the working face approaches, exceeding those in the roof, and then decrease away from it. The orientation of the $\sigma_1$ vector also rotates in this case from its initial horizontal position, perpendicular to the tunnel axis, to a horizontal position parallel to the tunnel axis. A second rotation occurs after the face advances 5 m past the monitoring point, to that of a vertical alignment tangential to the tunnel wall (as it would appear in a two-dimensional stress analysis).

In Case IV, where the primary $\sigma_{1i}$ is aligned parallel to the tunnel axis (i.e. $\sigma_{1i}$ and $\sigma_{2i}$ are reversed from those in Case III), results generally show similar trends but the deviatoric stress magnitudes and principal stress orientations vary (Fig. 10). Although values of $\sigma_2$ and $\sigma_3$ closely resemble those in Case III, the $\sigma_1$ stresses acting
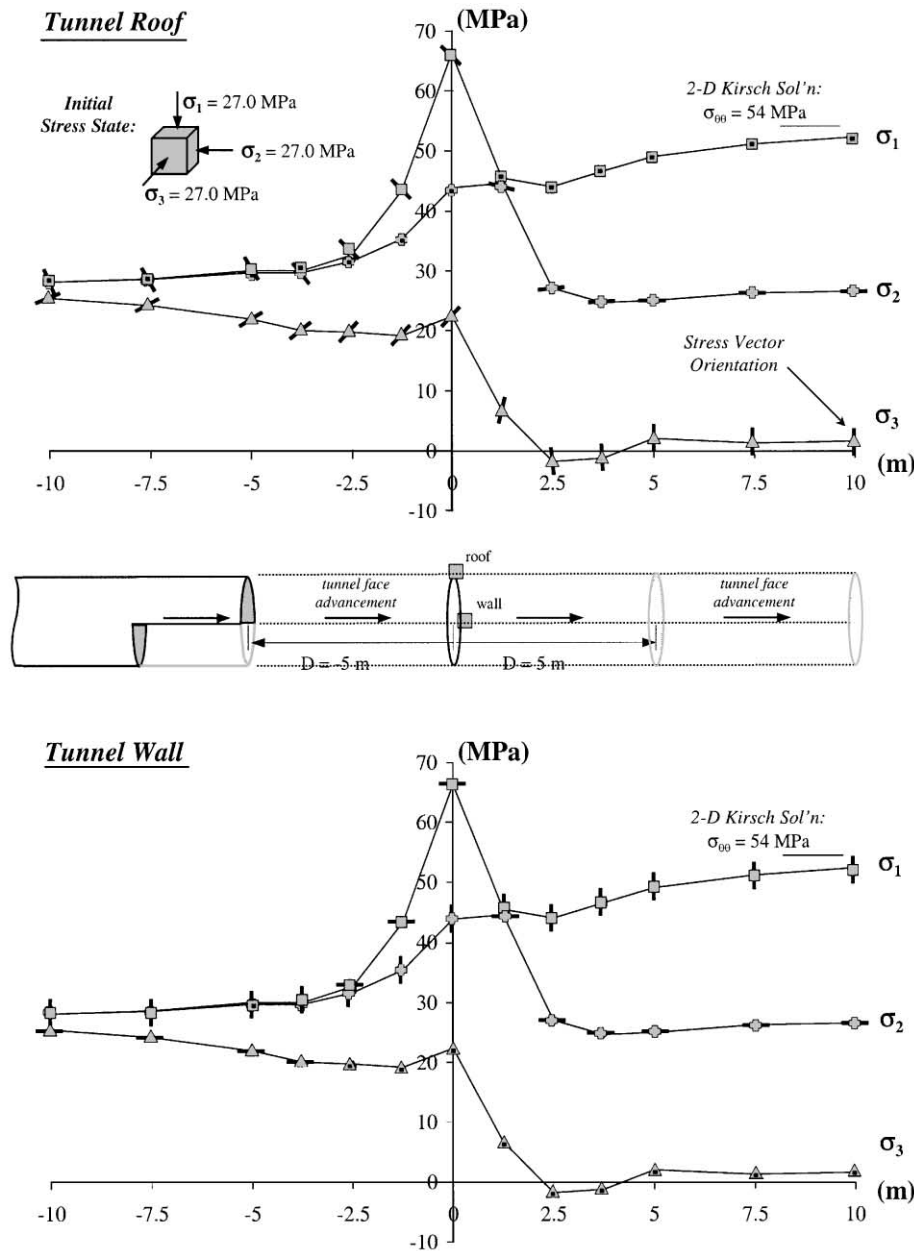
Fig. 8. Stress path plots of the principal stress magnitudes and orientations at fixed points in the tunnel roof (upper) and wall (lower) for initial stress state "Case II"—hydrostatic loading.

along the tunnel roof in Case IV sharply increase as the advancing tunnel face reaches the monitoring point exceeding values recorded for Case III. The orientation of the $\sigma_1$ stress vector at the monitoring point in the tunnel roof rotates from its initial position parallel to the tunnel axis, to that tilting vertically upwards as the tunnel face approaches. Once the tunnel face passes by, the $\sigma_1$ axis continues to rotate into a horizontal position perpendicular to the tunnel axis (Fig. 10, upper plot). The opposite occurs in the tunnel walls where the $\sigma_1$ stress trajectory rotates within a horizontal plane around the tunnel face as it approaches and passes by

the monitoring point, but then returns to its initial orientation parallel to the tunnel axis once the tunnel face advances several meters ahead of it.

### 3.2.2. Elasto-plastic yielding and stress redistribution

A key advantage of three-dimensional finite-element analysis compared to that of most three-dimensional boundary-element solutions is the ability to model elasto-plastic material yield. With an elastic solution, whether it is boundary-element or finite-element, the deviatoric stresses are a maximum at the excavation boundary and are unlimited in terms of the magnitudes
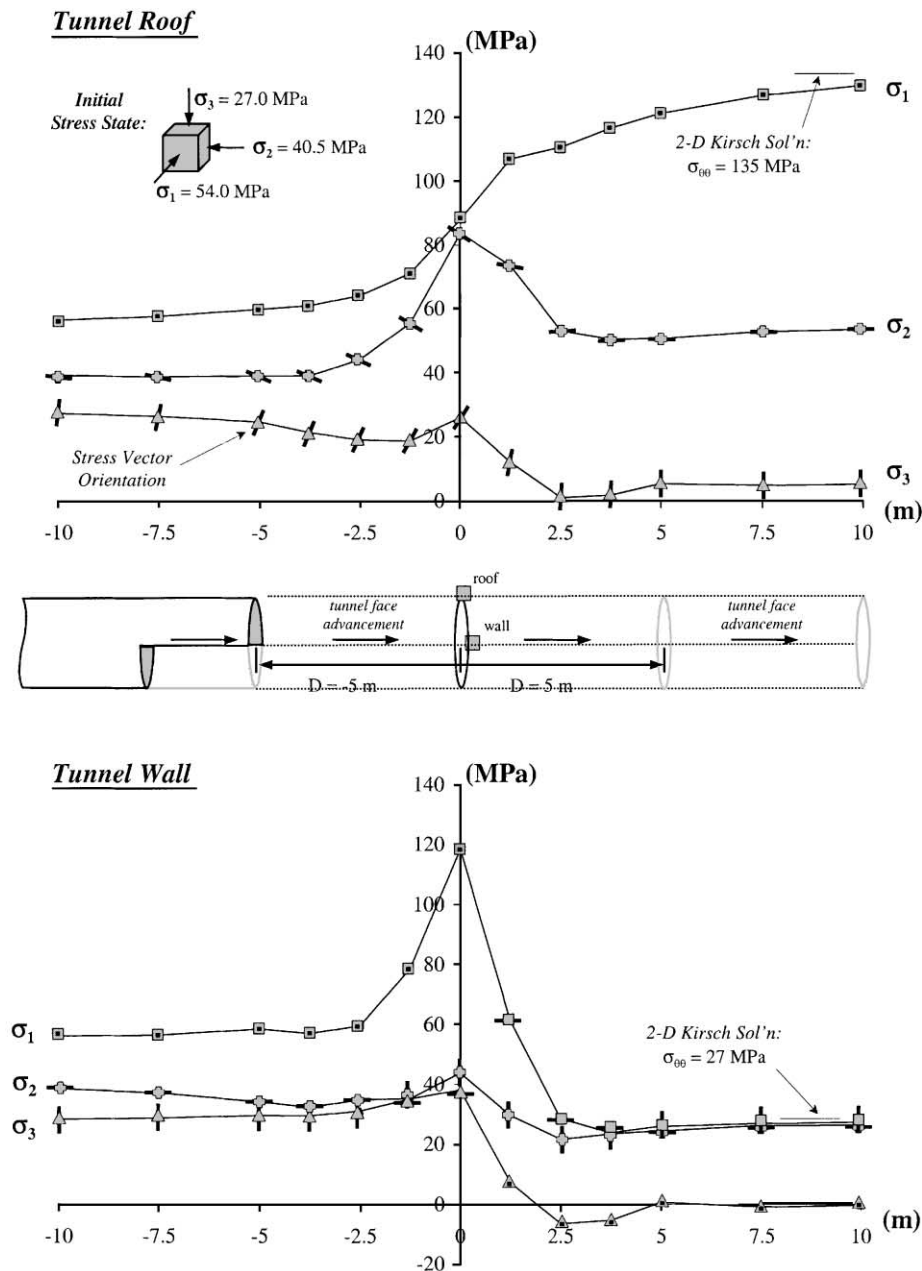
Fig. 9. Stress path plots of the principal stress magnitudes and orientations at fixed points in the tunnel roof (upper) and wall (lower) for initial stress state "Case III"—$\sigma_{1i}$ horizontal and perpendicular to tunnel axis.

they may reach. More realistically, however, rock will yield under high stresses resulting in a redistribution of the stresses away from the tunnel boundary. Panet [21] notes that in such cases, it is important to distinguish whether the plastic zone develops along the tunnel periphery behind the excavation face, or whether it encircles the excavation face thus endangering the stability of the face.

Numerous solutions have been developed to simulate material yield and for this study a Mohr–Coulomb elasto-plastic/visco-plastic constitutive relationship was used to model yield deformations under high stresses. A comparison between deviatoric stresses at the tunnel face calculated assuming linear elasticity and elasto-plastic yielding are shown in Fig. 11 for the initial stress conditions given for Case III. These results show that the stresses in the elasto-plastic model are significantly lower along the tunnel roof, where the zone of yield extends approximately 2 m, or 0.2 tunnel diameters, from the tunnel boundary. Moving outwards from the yielded zone, i.e. between 2 to 5 m from the tunnel boundary, stresses are higher than in the elastic model due to the shedding of stresses outwards from the inner yielded elements.
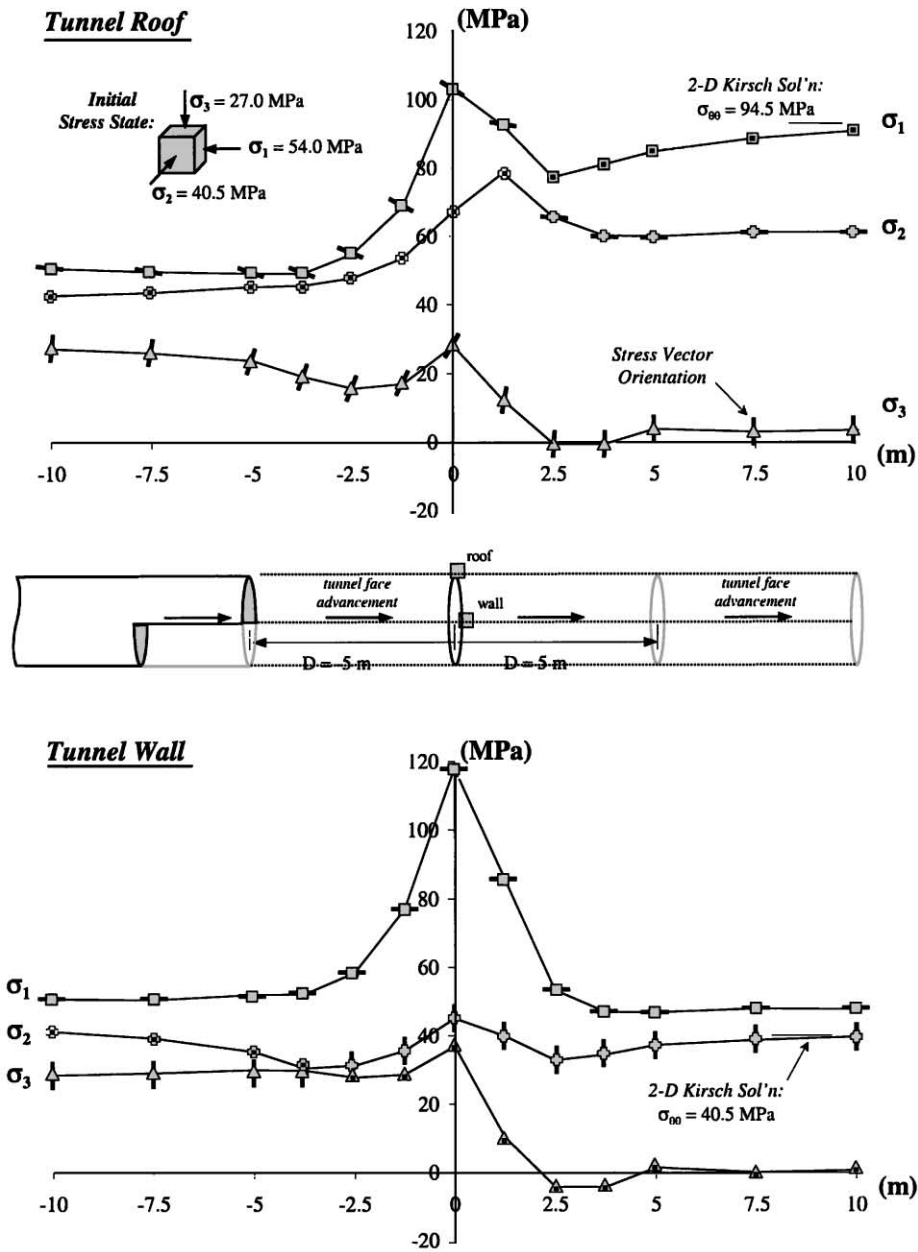
Fig. 10. Stress path plots of the principal stress magnitudes and orientations at fixed points in the tunnel roof (upper) and wall (lower) for initial stress state "Case IV"—$\sigma_{1i}$ parallel to tunnel axis.

Examination of the stress paths in Fig. 12 show that the principal stress magnitudes for the fixed tunnel roof monitoring point increase as the tunnel face approaches and then sharply drop off after the face advances past due to yielding along the tunnel boundary. This effect, however, is only seen in the $\sigma_1$ component of the stress tensor as the $\sigma_2$ and $\sigma_3$ stresses closely resemble those for the elastic case, both in terms of magnitude and orientation (plots for the equivalent elastic case are given in Fig. 9). The same can be seen in the plots for the near-field stresses in the tunnel walls where the results for the elasto-plastic case closely resemble those for the

elastic cases. However, plastic displacements do accumulate within the tunnel walls and even exceed those observed along the roof as shown in Fig. 13. Examination of the plastic component of displacement show that values significantly increase once the tunnel face advances beyond the monitoring points and the rock mass is left unconfined. The directional component, as illustrated in the plots, show that the total displacements point sharply towards the working face as it approaches the monitoring points and rotate into a perpendicular position towards the central tunnel axis once the tunnel face passes by.
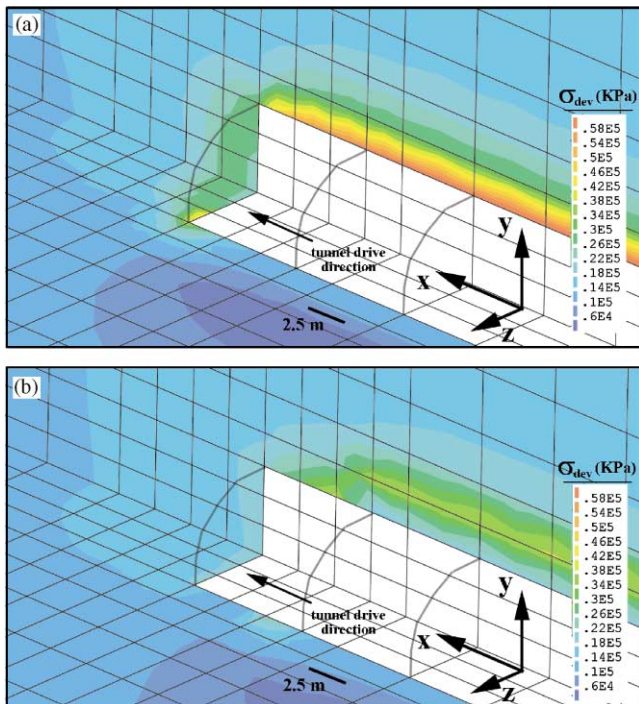
Fig. 11. Plots of the deviatoric stress contours, $\sigma_{dev}$, along the longitudinal tunnel profile assuming linear elasticity (upper) and elasto-plastic yielding (lower), for initial stress state "Case III".

A direct comparison between the elastic and elasto-plastic $\sigma_1$ stress paths for the tunnel roof monitoring point is provided in Fig. 14. From the stress path plots in Figs. 9, 12 and 14, results suggest that plastic yielding had only a minor effect with respect to altering the orientation of the principal stress axes. However, several minor deviations and rotations do occur as a result of elasto-plastic yielding, relative to the elastic examples, most notably along the tunnel walls when the position of the tunnel face coincides with the fixed monitoring point.

## 4. Stress path and evolution ahead of an advancing tunnel face—discussion

The preceding analyses demonstrate that the principal stresses ahead of a working tunnel face are constantly changing, both in terms of magnitude and orientation, during tunnel excavation. Studies by Read et al. [13] have shown that such three-dimensional effects can contribute to the development of brittle breakouts along the excavation boundary under high stress conditions. Furthermore, their results revealed that the extent and symmetry/asymmetry of the breakout pattern was partly controlled by the alignment of the principal stress axes relative to that of the excavation. These type of in situ observations sub-stantiate that failure, in highly stressed brittle rock masses, generally begins with the initiation and propagation of microfractures resulting in a conti-nuous degradation of the rock mass strength (as long as a critical imbalance in the energy of the system exists).

In the central Swiss Alps, where construction of the 57 km long Alptransit Gotthard base tunnel is currently under way, examples of brittle fracture-controlled instabilities have been observed in several existing tunnels (e.g. Furka tunnel, Gotthard road tunnel). Given the close proximity of these tunnels to the planned route of the new base-tunnel, similar processes may be expected leading to ground control difficulties. The Gotthard base tunnel will consist of two single-track tunnels approximately 10 m in diameter and separated 30 m horizontally from one another. Scheduled for completion in the year 2010, the tunnel will pass through the same granitic and gneissic formations as the Furka tunnel and Gotthard road tunnel but at significantly greater depths. In the Furka tunnel, signs of stress-induced brittle fracturing in the form of minor break-outs along the tunnel boundary and major spalling can be observed and still continues along an access tunnel, the 5200 m long "Fenster Bedretto", abandoned during construction (Figs. 15 and 16). With the maximum overburden above these sections reaching 1200 m, stress-induced instabilities in the Gotthard base tunnel are likely to be much more severe as the overburden will reach heights of 2500 m. Given the significant increase in overburden load, more violent stress-/fracture-controlled failures in the form of rockbursting can be expected [6].

The initiation and propagation of brittle fractures dominating such failure processes (i.e. spalling, rock-bursting, etc.), are themselves largely controlled by the stress magnitudes and orientation of the principal stress axes. In terms of magnitude, Martin [5] suggests that in situ brittle fracturing begins when the maximum deviatoric stress exceeds approximately one third the unconfined compressive strength of the intact rock. This corresponds to the crack initiation threshold, $\sigma_{ci}$, in crystalline materials as determined through laboratory testing [22]. These studies have shown that as stress magnitude increase, several subsequent stages of frac-ture development occur involving the initiation, propa-gation and coalescence of new and pre-existing fractures. In terms of orientation, numerous studies have shown that the propagation of these fracture systems occur in a preferential direction parallel to the major principal stress, $\sigma_1$. Furthermore, those micro-fractures not aligned with $\sigma_1$ but which are at angles where critical stress concentrations occur on their boundaries, grow along a curved path to align themselves with $\sigma_1$ [23–26].
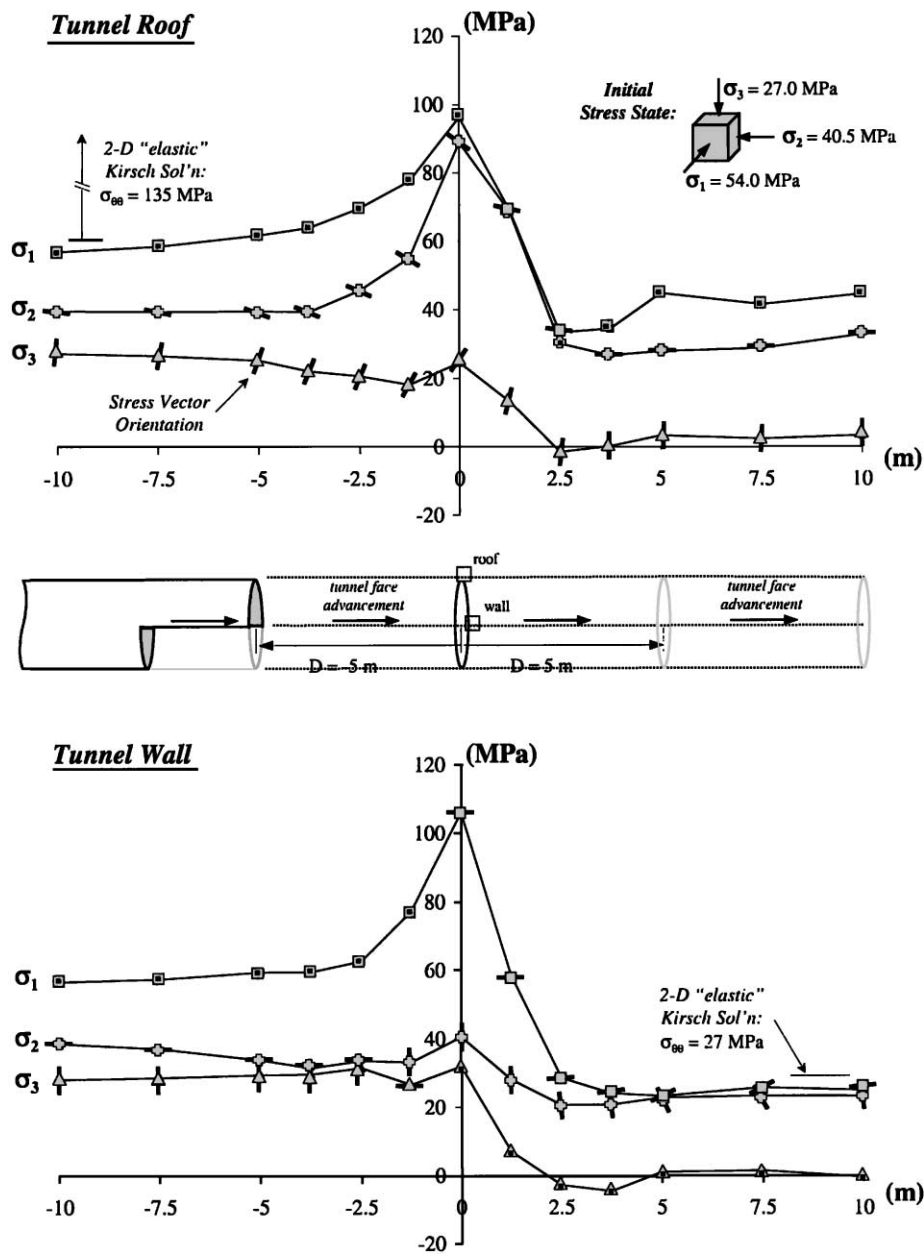
Fig. 12. Stress path plots of the principal stress magnitudes and orientations at fixed points in the tunnel roof (upper) and wall (lower) for initial stress state "Case III" with elasto-plastic material yield.

In the case of a circular tunnel, the excavation process reduces the confining pressure along the tunnel periphery and tangential stresses increase such that $\sigma_1$ orientates itself parallel to the tunnel boundary. Under high stress conditions, these stress concentrations results in the development of a process zone which further develops into unstable spalling of rock slabs one to several centimetres in thickness [27]. Similar examples from the Furka access tunnel, "Fenster Bedretto" (Figs. 17a and b), also show that pieces of failed/spalled rock are shaped by closely spaced brittle fractures propagating in the $\sigma_1$ direction tangential to the tunnel boundary. The thin rock slab pictured in Fig. 17b (which is 50 cm long but less than 2 cm thick) even retains the curvature of the circular tunnel wall. Martin [5] further notes that the processes driving these rock mass instabilities are three-dimensional in nature and initiate ahead of the tunnel face where stress concentrations induce brittle microfracturing and damage of the intact rock in the form of cohesion loss. In this sense, the accumulation of brittle fracture damage acts to irreversibly alter the strength and deformation characteristics of the rock [28], thus directly influencing rock mass instability.
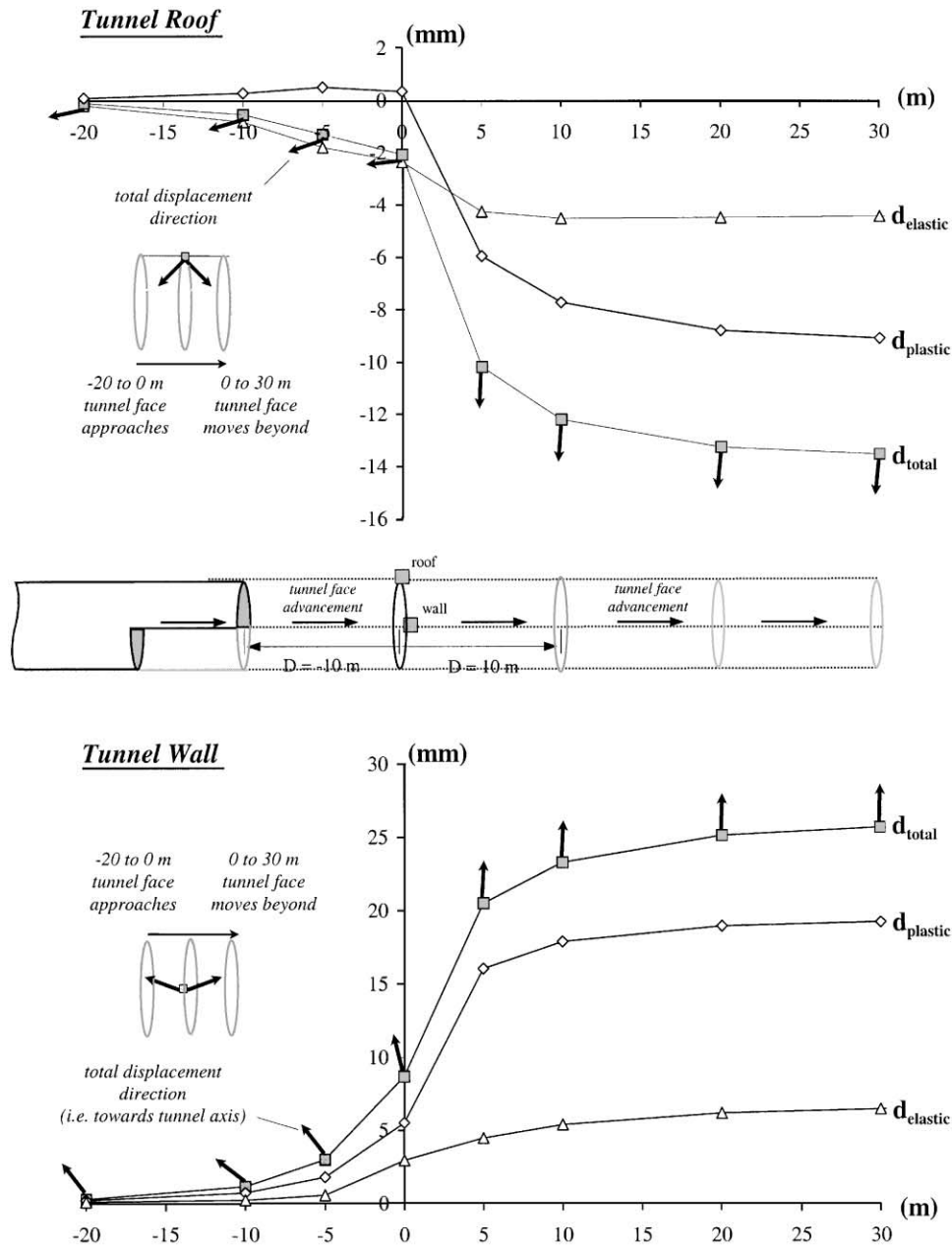
Fig. 13. Accumulation of elastic, plastic and total displacements with each tunnel face advance for fixed points in the tunnel roof (upper) and wall (lower) assuming the initial stress conditions for "Case III". Direction vectors are provided for the total displacements.

## 4.1. Spatial and temporal evolution of the three-dimensional stress field

Given the dependence of brittle microfracturing and damage on stress path, it becomes important to understand the spatial and temporal evolution of the three-dimensional stress field during the progressive excavation of the tunnel. One way of quantifying this is by assessing a brittle fracture damage indicator, either through complex constitutive relationships, mixed-mode fracture criteria or by use of an equivalent parameter. For example, material yield and/or the plastic component of strain represent irreversible damage to the rock mass as would result from the increasing initiation and development of stress-induced microfracturing. Fig. 18 demonstrates the accumulation of plastic strain in the rock mass as the tunnel face advances towards two fixed monitoring points for the conditions described in Section 3.2.2 on elasto-plastic modelling. However, this analysis only considers temporal changes to the rock mass resulting from increased stress magnitudes. Conceptually, and of equal interest, is how the directional propagation of the stress-induced brittle microfractures in the damage zone contribute to rock mass strength degradation and the resulting failure mechanism.
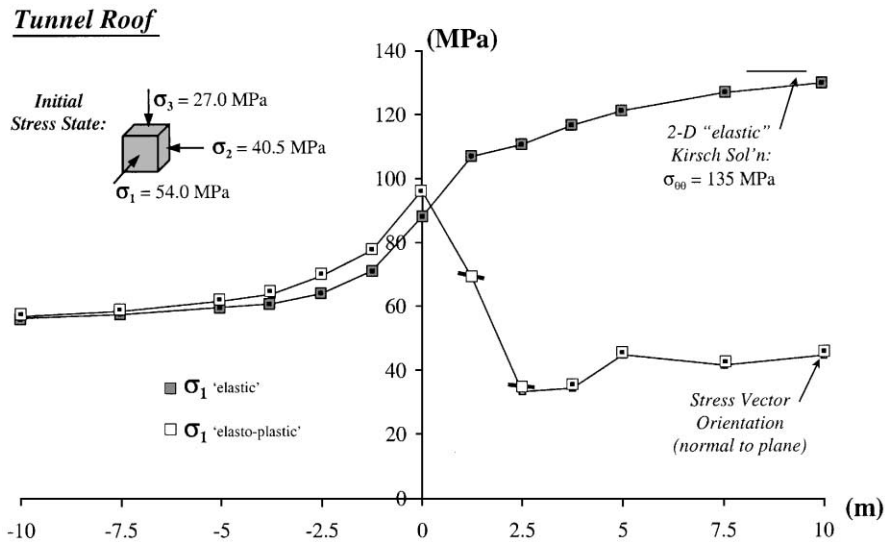
Fig. 14. Comparison of $\sigma_1$ stress magnitudes and orientations, at fixed points in the tunnel roof boundary, resulting from linear elastic conditions and elasto-plastic yielding.



Fig. 15. Stress-induced breakout and notch formation along the roof of the Furka access tunnel "Fenster Bedretto".
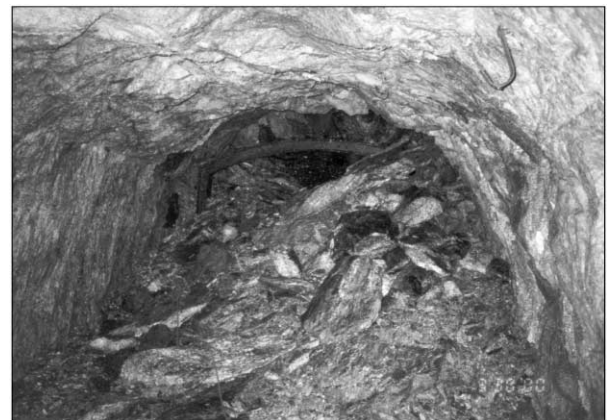


Fig. 16. Major brittle spalling along an abandoned section of the Furka access tunnel "Fenster Bedretto".

Finite-element analysis in the preceding sections focused on the continuous evolution of both the principal stress distribution and their axis orientations. As such, for a given unit volume of rock positioned ahead of the tunnel face, the rock will experience a series of stress increases and/or decreases as well as several rotations of the principal stress axes with each advancement of the tunnel face. Fig. 19 presents a temporal representation of the stress analysis shown in Fig. 6 (i.e. initial stress state Case I), where "snapshots" of the principal stress magnitudes and axes orientations are shown for several stages of tunnel development as the excavation approaches and passes through a unit volume of rock. From this analysis, it can be seen that the $\sigma_1$ axis eventually rotates 90° from it's original orientation and the deviatoric stress doubles as the tunnel approaches the monitoring point before dropping to one fifth of its original value after the tunnel passes by

it. These results vary depending on the initial magnitudes and alignment of the far-field principal stress axes (e.g. vertical or horizontal) but do help to illustrate that $\sigma_1$, the preferred direction of fracture propagation, widely varies in time during advancement of the tunnel face.

If the excavation-induced stresses in a representative unit volume of rock exceeds the crack initiation threshold, then what can be said about the direction of fracture propagation and the accumulation of brittle fracture damage? Wu and Pollard [29] have shown through laboratory testing that secondary fractures can initiate and propagate from a set of primary fractures in a new direction parallel to the new $\sigma_1$, if the remote stress field changes orientation. Fracture geometry, spacing and stress field orientation then controls the extent to which these secondary fractures develop. Thus, it can be generally assumed that as the $\sigma_1$ stress axis
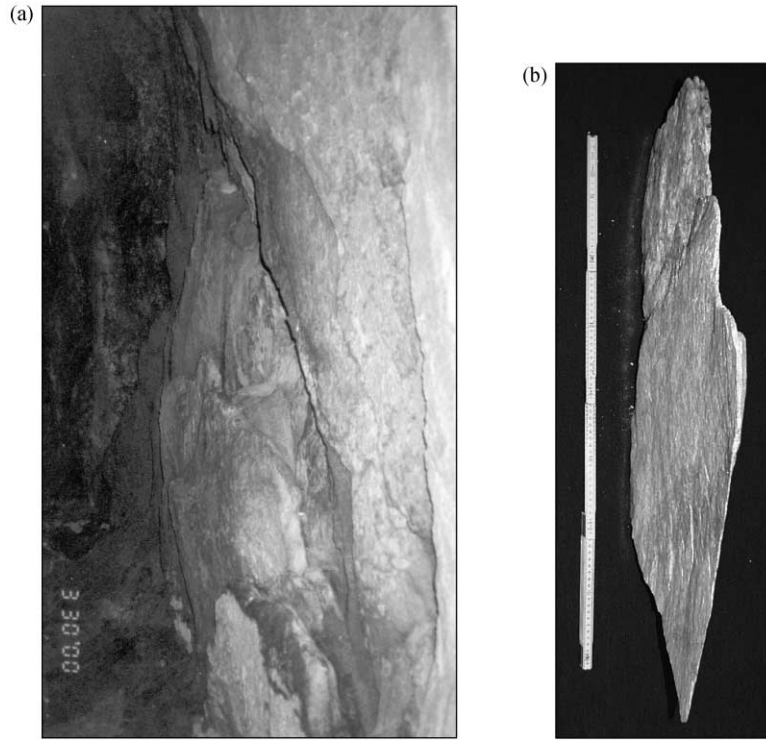
Fig. 17. Thin granite slabs shaped by stress-induced brittle fractures propagating parallel to the tunnel boundary. (a) in situ development—Furka access tunnel "Fenster Bedretto"; (b) thin slab 50 cm long but less than 2 cm thick retaining curvature of the circular tunnel wall.
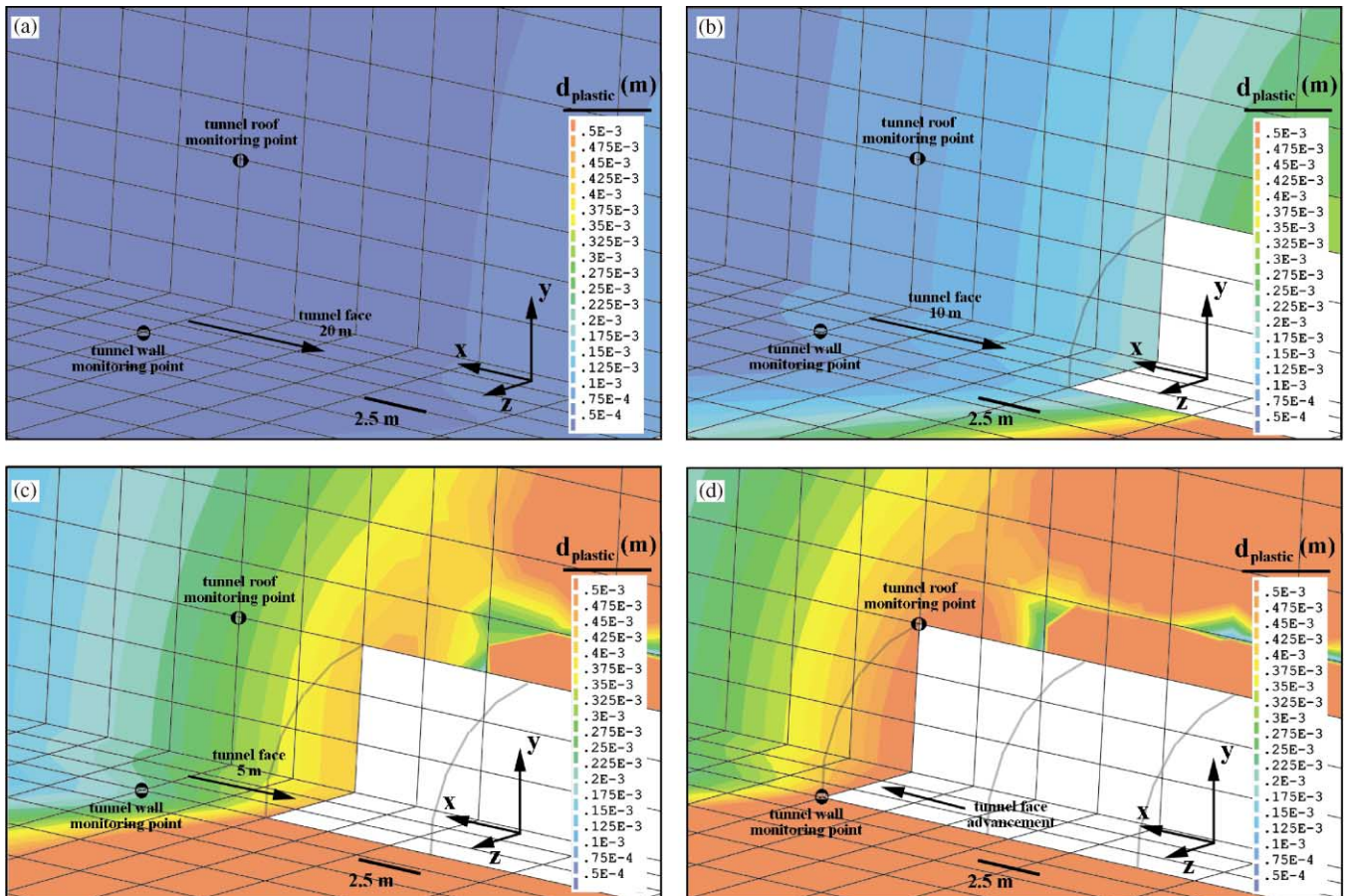


Fig. 18. Contours of cumulative plastic displacements during advancement of the tunnel face relative to the position of fixed monitoring points at: (a) 20 m away; (b) 10 m away; (c) 5 m away; and (d) 0 m away.
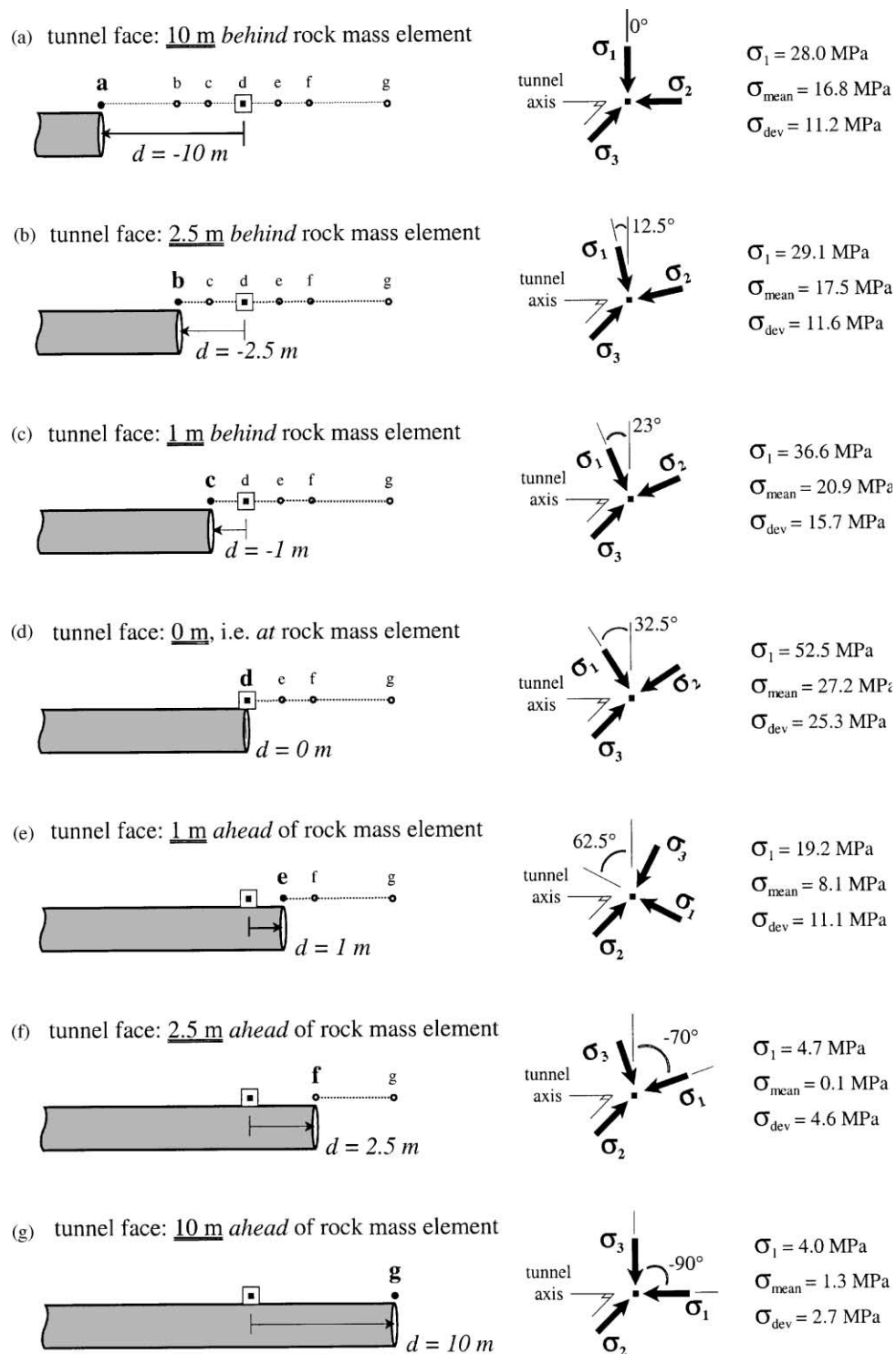
Fig. 19. Principal stress magnitudes and axes orientations showing stress rotation for several stages of tunnel development as the excavation approaches and passes through a unit volume of rock.

rotates, the fracture density and the degree of stress-induced brittle fracture damage increases as new microfractures initiate over a successive series of critical angles (Fig. 20). Increased microfracturing damage, however, does not necessarily correspond to increased

tunnel stability problems. This will depend on the extent that the fractures develop, which in turn will depend on the interaction between neighbouring propagating fractures relative to the applied stress field. Eberhardt et al. [30] demonstrated that as a set of fractures initiate and
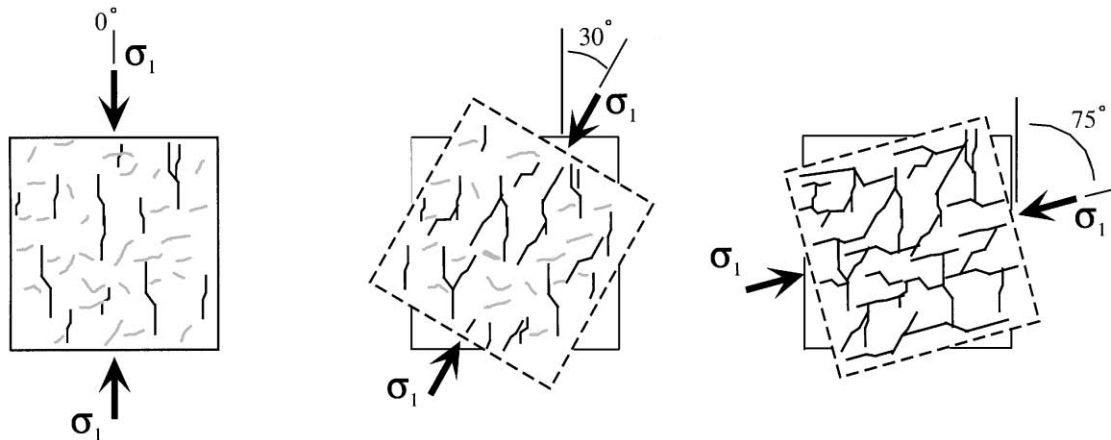
Fig. 20. Conceptual model of increased stress-induced brittle fracture damage due to rotation of the $\sigma_1$ stress axis over a successive series of critical angles.

propagate, and the localised stress concentrations surrounding their tips begin to interact with one another, neighbouring microfractures can act to either suppress or promote further fracture growth.

## 4.2. In situ stress state, fracture propagation and damage evolution

Read et al. [31] found that the tunnel orientation relative to the in situ principal stress axes can greatly affect the potential for such stress-induced damage in localised regions surrounding the tunnel. A summary of the results showing the degree of stress field rotation during the progressive excavation/advancement of the tunnel face for each of the initial stress cases, as described in Table 2, is presented in Table 3. For the first initial stress condition, i.e. Case I, where loading is lithostatic and $\sigma_{1i}$ is vertical, the highest deviatoric stresses will concentrate along the tunnel walls. However, inspection of the $\sigma_1$ stress vector within a rock element that is positioned along a line parallel to the tunnel's wall shows that the direction of $\sigma_1$ does not vary from that of $90°$ vertical as the tunnel face approaches and passes by it (Table 3). In other words, if the fracture initiation threshold is exceeded in this rock element, then fractures will only propagate in a direction tangential to the tunnel walls, as is the case in observations of spalling phenomenon (Fig. 17).

The same is true for the tunnel roof when the initial $\sigma_{1i}$ orientation is horizontal and perpendicular to the tunnel axis (Case III), i.e. the orientation of $\sigma_1$ does not vary from the tangential to the boundary and spalling conditions may prevail. In both cases, $\sigma_1$ rotation occurs only within rock elements positioned along portions of the tunnel boundary normal to the direction of the initial in situ $\sigma_{1i}$ stress (where the

corresponding deviatoric stresses are reduced). Thus, if the initial stress magnitudes are relatively high, as in Case III, the deviatoric stresses may be high enough to induce brittle fracture damage along these tunnel segments (e.g. in the tunnel walls of Case III). Although these processes may not lead directly to tunnel instability problems, they may contribute to different instability mechanisms over time. Similarly, microfracture propagation along several different directions within the same rock element may increase the microfracture connectivity and thus significantly increase the permeability of the near-field boundary rock, a major concern in the underground storage/disposal of hazardous waste.
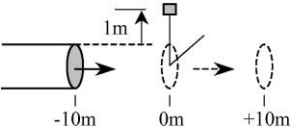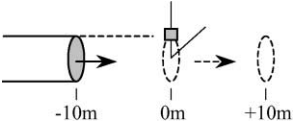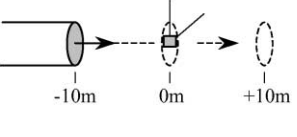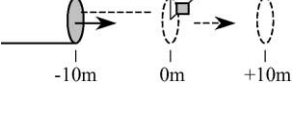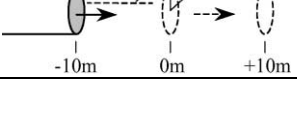
Under hydrostatic conditions, Case II, and in Case IV, where the initial $\sigma_{1i}$ stress is aligned parallel to the tunnel axis, both increases in deviatoric stresses and rotation of the $\sigma_1$ stress axis occur simultaneously in both the tunnel walls and roof. Further examination of the results presented in Table 3 show that these effects diminish as the position of the monitored unit volume of rock moves away from the tunnel boundary normal to the tunnel axis (e.g. $> 1$ m).

## 5. Conclusions

Results were presented from a detailed three-dimensional finite-element analysis directed towards resolving the complex spatial and temporal stress paths, which evolve ahead of an advancing tunnel face. Models were based on and examples taken from the planned Gotthard base tunnel and the existing Fenster Bedretto in the central Swiss Alps. Given the depth and expected high stress environment in the Gotthard base tunnel project, coupled with uncertainties involving the in situ stress state, understanding the

Table 3

Summary of results showing deviatoric stress magnitudes and rotation of the principal stress axis during the progressive advancement of the tunnel face. Initial stress conditions for Cases I–IV are described in Table 2. Trend is taken as the angle of rotation within a horizontal plane with respect to the tunnel axis; plunge is taken as the downward dip angle from horizontal

| Tunnel face position (m) | Case I | | | Case II | | | Case III | | | Case IV | | |
|---|---|---|---|---|---|---|---|---|---|---|---|---|
| | Deviatoric stress (MPa) | $\sigma_1$ Trend (°) | $\sigma_1$ Plunge (°) | Deviatoric stress (MPa) | $\sigma_1$ Trend (°) | $\sigma_1$ Plunge (°) | Deviatoric stress (MPa) | $\sigma_1$ Trend (°) | $\sigma_1$ Plunge (°) | Deviatoric stress (MPa) | $\sigma_1$ Trend (°) | $\sigma_1$ Plunge (°) |
| **1 m above roof line** | | | | | | | | | | | | |
| −10 | 11.1 | 0 | 88 | 0.9 | 89 | 3 | 15.2 | 90 | 0 | 11.0 | 0 | 5 |
| −2.5 | 12.1 | 0 | 79 | 3.6 | 5 | 43 | 19.2 | 90 | 0 | 15.5 | 1 | 16 |
| 0 | 16.9 | 0 | 58 | 10.6 | 0 | 39 | 20.0 | 90 | 0 | 21.2 | 0 | 20 |
| 2.5 | 3.4 | 0 | −15 | 13.5 | 90 | 0 | 35.9 | 90 | 0 | 17.6 | 1 | 3 |
| 10 | 2.4 | 90 | −2 | 18.5 | 90 | 0 | 45.0 | 90 | 0 | 24.6 | 90 | 0 |
| **Roof line** | | | | | | | | | | | | |
| −10 | 11.2 | 0 | 89 | 0.9 | 88 | 6 | 15.4 | 90 | 0 | 10.4 | 0 | 6 |
| −2.5 | 11.6 | 0 | 78 | 4.6 | 7 | 43 | 21.6 | 90 | 0 | 15.4 | 1 | 22 |
| −1.25 | 15.7 | 0 | 67 | 10.7 | 1 | 44 | 22.7 | 90 | 0 | 22.2 | 1 | 27 |
| 0 | 25.3 | 0 | 58 | 22.1 | 0 | 43 | 22.1 | 88 | 1 | 37.2 | 0 | 31 |
| 1.25 | 11.1 | 0 | 28 | 13.3 | 89 | 1 | 42.8 | 90 | 0 | 31.4 | 0 | 10 |
| 2.5 | 4.6 | 1 | −19 | 20.9 | 90 | 0 | 55.7 | 90 | 0 | 29.8 | 90 | 0 |
| 10 | 2.7 | 0 | 0 | 25.5 | 90 | 0 | 67.0 | 90 | 0 | 39.0 | 90 | 0 |
| **Center line** | | | | | | | | | | | | |
| −10 | 11.5 | — | 90 | 1.2 | 90 | 0 | 16.1 | 90 | 0 | 7.8 | 0 | 0 |
| −2.5 | 17.5 | — | 90 | 8.2 | 90 | 1 | 29.9 | 90 | 0 | 17.5 | 90 | 0 |
| −1.25 | 18.3 | — | 90 | 8.0 | 90 | 16 | 30.7 | 90 | 0 | 17.0 | 90 | 0 |
| 0 | 17.9 | — | 90 | 6.5 | 90 | 6 | 28.7 | 90 | 0 | 13.7 | 90 | 0 |
| **Wall line** | | | | | | | | | | | | |
| −10 | 11.3 | — | 90 | 0.9 | — | 90 | 15.1 | 85 | 0 | 10.6 | 15 | 0 |
| −2.5 | 14.2 | — | 90 | 4.6 | 43 | 0 | 17.8 | 63 | 0 | 19.3 | 33 | 0 |
| −1.25 | 15.4 | — | 90 | 10.7 | 44 | 0 | 29.2 | 56 | 0 | 29.9 | 37 | 0 |
| 0 | 17.0 | — | 90 | 22.1 | 43 | 0 | 51.6 | 50 | 0 | 51.3 | 39 | 0 |
| 1.25 | 26.5 | — | 90 | 13.3 | — | 90 | 28.6 | 19 | 0 | 40.6 | 13 | 0 |
| 2.5 | 32.1 | — | 90 | 21.0 | — | 90 | 14.0 | 6 | 0 | 26.0 | 5 | 0 |
| 10 | 37.8 | — | 90 | 25.5 | — | 90 | 9.5 | — | 90 | 18.3 | 0 | 0 |
| **1 m beyond wall line** | | | | | | | | | | | | |
| −10 | 25.5 | — | 90 | 0.9 | — | 90 | 14.9 | 85 | 0 | 11.1 | 13 | 0 |
| −2.5 | 21.3 | — | 90 | 3.6 | 43 | 0 | 17.4 | 67 | 0 | 17.6 | 29 | 0 |
| 0 | 14.6 | — | 90 | 10.6 | 40 | 0 | 31.4 | 50 | 0 | 30.7 | 33 | 0 |
| 2.5 | 13.2 | — | 90 | 13.5 | — | 90 | 12.0 | 8 | 0 | 23.6 | 5 | 0 |
| 10 | 11.1 | — | 90 | 18.5 | — | 90 | 10.4 | — | 90 | 17.7 | 0 | 0 |

influence of stress path on brittle failure mechanisms may prove essential during future construction and support considerations if unforeseen problems arise. Stress path analyses were therefore provided for several varying alignments of the initial in situ stress field relative to the tunnel axis.

Stress path effects were examined with respect to stress-induced brittle microfracturing and elasto-plastic yielding. The progressive accumulation of damage in front of an advancing tunnel face, in the form of irreversible elasto-plastic yielding, was presented based on conventional stress path analysis (i.e. focusing on changing stress magnitudes). However, and more central to the key emphasis of the paper, results were also analysed in terms of the rotation of the $\sigma_1$ trajectory at a fixed point with each advancement of an approaching tunnel face. Given the dependence of brittle fracture propagation on the orientation of the $\sigma_1$ stress axis, conceptual models were presented showing how such rotations may lead to different types of stress-induced damage, and therefore, different brittle failure mechanisms. Accordingly, modelled stress concentrations at the tunnel face were found to be highest in the walls and roof when the initial $\sigma_1$ stress was aligned vertically and horizontally perpendicular to the tunnel axis, respectively. However, no significant rotation of the $\sigma_1$ axis was observed in these cases thereby inferring that the propagating microfractures would proceed along a single path of development. These results provide key initial indicators as to the far field stress state existing over certain sections of the Fenster Bedretto where spalling-type processes dominate and fracture propagation occurs primarily tangential to the tunnel boundary walls. Alternatively, high stress concentrations in association with large rotations of the $\sigma_1$ stress axis were observed when the initial $\sigma_1$ alignment was horizontal and parallel to the tunnel axis. In such cases, brittle fracture propagation becomes more complex, leading to increased damage in the excavation disturbed zone ahead of and surrounding the tunnel periphery.

Results show that both the consideration of stress magnitudes, as routinely performed in conventional stress path analyses, and the rotation of the principal stress axes, which in turn controls the preferred direction for fracture propagation, are necessary to transcend a phenomenological understanding of brittle fracture damage and failure. Such insights would prove valuable for the design of stable tunnels in high stress environments, like those that will be encountered during the construction of the Gotthard base tunnel. Similar concerns in mining, deep borehole drilling and nuclear waste disposal would also be addressed through a better understanding as to the role stress rotation and brittle fracture damage plays in the degradation of the near-field rock strength and permeability.

## References

[1] Eberhardt E, Stead D, Reeves MJ, Connors C. Design of tabular excavations in foliated rock: an integrated numerical modelling approach. Geotech Geol Engng 1997;15(1):47–85.

[2] Meyer LHI, Stead D, Coggan JS. Three dimensional modelling of the effects of high horizontal stress on underground excavation stability. In: Vouille G, Berest P, editors. Proceedings of the Ninth International Congress on Rock Mechanics, Paris. Rotterdam: A.A. Balkema, 1999. p. 411–16.

[3] Abel JF, Lee FT. Stress changes ahead of an advancing tunnel. Int J Rock Mech Min Sci Geomech Abstr 1973;10(6):673–97.

[4] Seki J, Noda K, Washizawa E, Suzuki T, Nishino K. Effect of bench length on stability of tunnel face. In Abdel-Salam ME, editor. Proceedings of the International Congress on Tunnelling and Ground Conditions, Cairo. Rotterdam: A.A. Balkema, 1994. p. 531–42.

[5] Martin CD. Seventeenth Canadian Geotechnical Colloquium: The effect of cohesion loss and stress path on brittle rock strength. Can Geotech J 1997;34(5):698–725.

[6] Loew S, Ziegler H-J, Keller F. Alptransit: Engineering geology of the world's longest tunnel system. In: GeoEng 2000 Proceedings, International Conference on Geotechnical & Geological Engineering, Melbourne. Lancaster: Technomic Publishing, 2000. p. 927–37.

[7] Duddeck H. Application of numerical analysis for tunnelling. Int J Numer Anal Methods Geomech 1991;15(4):223–39.

[8] Pan XD, Hudson JA. Plane strain analysis in modelling three-dimensional tunnel excavations. Int J Rock Mech Min Sci Geomech Abstr 1988;25(5):331–7.

[9] Kielbassa S, Duddeck H. Stress-strain fields at the tunnelling face—Three-dimensional analysis for two-dimensional technical approach. Rock Mech Rock Engng 1991;24(3):115–32.

[10] Panet M, Guenot A. Analysis of convergence behind the face of a tunnel. In: Jones MJ, editor. Tunnelling '82: Third International Symposium, Brighton. London: The Institution of Mining and Metallurgy, 1982. p. 197–204.

[11] Swoboda G, Mertz W, Schmid A. Three-dimensional numerical models to simulate tunnel excavation. In: Pietruszczak S, Pande GN, editors. Proceedings of the Third International Symposium on Numerical Models in Geomechanics (NUMOG III), Niagra Falls. London: Elsevier Applied Science, 1989. p. 536–48.

[12] Renato EB, Karel R. Tunnel design and construction in extremely difficult ground conditions. Tunnel 1998;8/98:23–31.

[13] Read RS, Martin CD, Dzik EJ. Asymmetric borehole breakouts at the URL. In: Daemen JJK, Schultz RA, editors. Rock Mechanics, Proceedings of the 35th US Symposium, Reno. Rotterdam: A.A. Balkema, 1995. p. 879–84.

[14] Schubert W, Budil A. The importance of longitudinal deformation in tunnel excavation. In: Fujii T, editor. Proceedings of the Eighth International Congress on Rock Mechanics, Tokyo. Rotterdam: A.A. Balkema, 1995. p. 1411–14.

[15] Martin CD, Read RS, Dzik EJ. Near-face cracking and strength around underground openings. In: Rossmanith H-P, editor.

Proceedings of the Second International Conference on the Mechanics of Jointed and Faulted Rock, Vienna. Rotterdam: A.A. Balkema, 1995. p. 765–70.

[16] VIPS. Vectorial Implementation of Structural Analysis and Geotechnical Engineering (VISAGE), version 7.4. Windsor: Vector International Processing Systems Limited, 2000.

[17] Keller F, Wanner H, Schneider TR. Geologischer schlussbericht Gotthard-Strassentunnel. Bern: Schweizerischen Geotechnischen Kommission, vol. 70, 1987.

[18] Carter BJ. Size and stress gradient effects on fracture around cavities. Rock Mech Rock Engng 1992;25(3):167–86.

[19] Germanovich LN, Dyskin AV. Fracture mechanisms and instability of openings in compression. Int J Rock Mech Min Sci 2000;37(1-2):263–84.

[20] Brady BHG, Brown ET. Rock mechanics for underground mining. London: Chapman & Hall, 1993.

[21] Panet M. Understanding deformations in tunnels. In: Hudson JA, editor. Comprehensive rock engineering principles, practice and projects 1. New York: Pergamon Press, 1993. p. 663–90.

[22] Eberhardt E, Stead D, Stimpson B, Read RS. Identifying crack initiation and propagation thresholds in brittle rock. Can Geotech J 1998;35(2):222–33.

[23] Hoek E, Bieniawski ZT. Brittle fracture propagation in rock under compression. Int J Frac Mech 1965;1(3):137–55.

[24] Lajtai EZ. A theoretical and experimental evaluation of the Griffith theory of brittle fracture. Tectonophysics 1971;11:129–56.

[25] Peng S, Johnson AM. Crack growth and faulting in cylindrical specimens of Chelmsford granite. Int J Rock Mech Min Sci Geomech Abstr 1972;9(1):37–86.

[26] Huang J, Wang Z, Zhao Y. The development of rock fracture from microfracturing to main fracture formation. Int J Rock Mech Min Sci Geomech Abstr 1993;30(7):925–8.

[27] Martin CD, Read RS, Martino JB. Observations of brittle failure around a circular test tunnel. Int J Rock Mech Min Sci 1997;34(7):1065–73.

[28] Eberhardt E, Stead D, Stimpson B. Quantifying progressive pre-peak brittle fracture damage in rock during uniaxial compression. Int J Rock Mech Min Sci 1999;36(3):361–80.

[29] Wu H, Pollard DD. Possible secondary fracture patterns due to a change in the direction of loading. In: Myer LR, Cook NGW, Goodman RE, Tsang C-F, editors. Proceedings of the Conference on Fractured and Jointed Rock Masses, Lake Tahoe. Rotterdam: A.A. Balkema, 1995. p. 487–93.

[30] Eberhardt E, Stead D, Stimpson B, Lajtai EZ. The effect of neighbouring cracks on elliptical crack initiation and propagation in uniaxial and triaxial stress fields. Engng Frac Mech 1998;59(2):103–15.

[31] Read RS, Chandler NA, Dzik EJ. In situ strength criteria for tunnel design in highly-stressed rock masses. Int J Rock Mech Min Sci 1998;35(3):261–78.